



# Influence of molar ratio and calcination temperature on the properties of $\text{Ti}_x\text{Sn}_{1-x}\text{O}_2$ supporting copper oxide for CO oxidation

Lihui Dong<sup>a</sup>, Yanxia Tang<sup>a</sup>, Bin Li<sup>a</sup>, Liya Zhou<sup>a</sup>, Fuzhong Gong<sup>a</sup>, Haixiang He<sup>a</sup>,  
 Baozhen Sun<sup>a</sup>, Changjin Tang<sup>b</sup>, Fei Gao<sup>c</sup>, Lin Dong<sup>b,c,\*</sup>

<sup>a</sup> Guangxi Key Laboratory of Petrochemical Resource Processing and Process Intensification Technology, School of Chemistry and Chemical Engineering, Guangxi University, Nanning 530004, PR China

<sup>b</sup> Key Laboratory of Mesoscopic Chemistry of MOE, School of Chemistry and Chemical Engineering, Nanjing University, Nanjing 210093, PR China

<sup>c</sup> Center of Modern Analysis, Nanjing University, Nanjing 210093, PR China

## ARTICLE INFO

### Article history:

Received 11 February 2015

Received in revised form 17 June 2015

Accepted 18 June 2015

Available online 4 July 2015

### Keywords:

Copper oxide

$\text{TiO}_2$ – $\text{SnO}_2$  mixed oxide

In situ IR

CO oxidation

Reaction mechanism

## ABSTRACT

$\text{Ti}_x\text{Sn}_{1-x}\text{O}_2$  mixed oxides were synthesized by the coprecipitation method.  $\text{CuO}/\text{Ti}_x\text{Sn}_{1-x}\text{O}_2$  catalysts were then prepared by wetness impregnation of the mixed oxides with  $\text{Cu}(\text{NO}_3)_2$ . These catalysts were characterized using X-ray diffraction (XRD), laser Raman spectroscopy (LRS),  $\text{H}_2$ -temperature-programmed reduction (TPR),  $\text{O}_2$ -temperature-programmed desorption (TPD), X-ray photoelectron spectroscopy (XPS), and in situ Fourier transform infrared (FT-IR) techniques. The activities of the catalysts during CO oxidation were evaluated. The following observations were made: (1) CuO species can be highly dispersed on the  $\text{Ti}_x\text{Sn}_{1-x}\text{O}_2$  supports, such that several surface  $\text{Cu}^+$  ions and oxygen vacancies are formed. (2) Among the prepared catalysts, the  $5\text{CuO}/\text{Ti}_{0.75}\text{Sn}_{0.25}\text{O}_2$ -600 °C catalyst exhibits the highest reducing property, which arises from the difference in electronegativity between Ti and Sn. (3) The CO species can adsorb on  $\text{Cu}^+$  and  $\text{O}_2$  on the oxygen vacancy, which forms  $\text{O}_2^-$  species. The in situ FT-IR results show that the  $\text{Cu}^+-(\text{CO})_2$  species and  $\text{O}_2^-$  adsorbed on the catalyst play a key role in CO oxidation. (4) The resistance of the catalysts to  $\text{H}_2\text{O}$  is related to the Brunauer–Emmett–Teller (BET) surface area and the  $\text{H}_2\text{O}$  adsorption on the catalyst surface. Furthermore, a possible reaction mechanism is tentatively proposed to understand this reaction.

© 2015 Elsevier B.V. All rights reserved.

## 1. Introduction

The catalytic oxidation of carbon monoxide has been of considerable interest because of its significance in deep sea diving, human safety measures in mines, space exploration, CO sensing, and air cleaning [1,2]. Moreover, CO oxidation is a side reaction observed in some industrial processes such as methanol production [3] and water–gas shift reaction [4–6]. Noble metal-based catalysts are efficient for low-temperature CO oxidation [7–9], but the high cost of precious metals limits their applications. Thus, researchers have turned to the study of non-noble metal-based catalysts, especially copper oxide [10–12]. Although supported copper oxides [13–23] are highly active for CO oxidation, the reaction usually takes place at elevated temperatures (>200 °C). The systems of interests include  $\text{CuO}/\text{CeO}_2$  [13–15,18–20],  $\text{CuO}/\text{TiO}_2$  [21–23],  $\text{CuO}/\text{SnO}_2$  [15,16],

$\text{CuO}/\text{Al}_2\text{O}_3$  [24,25], etc. Among these,  $\text{CuO}/\text{TiO}_2$  catalysts have been studied intensively because they show promising activity for CO oxidation [21–23]. However, pure  $\text{TiO}_2$  is reported to have poor thermal stability [26]. Tin is widely used to improve the stability of  $\text{TiO}_2$ .  $\text{TiO}_2$ – $\text{SnO}_2$  mixed oxides are more resistant to thermal aging and better redox agents than pure  $\text{TiO}_2$ , because the  $\text{Sn}^{4+} \rightarrow \text{Sn}^{2+}$  reaction occurs at relatively lower temperatures [27,28]. Recent studies have found that copper oxide supported on  $\text{TiO}_2$ – $\text{SnO}_2$  mixed oxide is more favorable for CO oxidation than those supported on pure  $\text{TiO}_2$  and  $\text{SnO}_2$  [29,30]. However, the intrinsic factors that enhance these activities is still not clear. Specifically, the effect of the Ti/Sn ratio and the thermal treatment of the mixed oxide on the catalyst activity remains to be studied.

Previous research has focused on correlating the surface structure and composition of supported CuO catalysts with their catalytic behavior [13–34], thus suggesting that the locus of catalytic activity for CO oxidation is a copper center. Although supported oxidic [13–25] and metallic [31,32] copper catalysts have been studied frequently and extensively, the specific nature of the active sites is still uncertain. In these studies, highly dispersed sur-

\* Corresponding author at: 22# Hankou road, Nanjing University, Nanjing 210093, Jiangsu province, PR China. Fax: +86 25 83317761.

E-mail address: [donglin@nju.edu.cn](mailto:donglin@nju.edu.cn) (L. Dong).

face  $\text{Cu}^+$  species are reported to be the most active compared with  $\text{Cu}^{2+}$  and  $\text{Cu}^0$  [11,13,25,33,34]. Lopez Agudo studied CO oxidation over alumina-supported copper oxide catalysts and found that  $\text{Cu}^+$  and/or  $\text{Cu}^0$  were the active sites for CO oxidation [35]. Jernigan and Somorjai [36] showed that the rate of CO oxidation at 300 °C decreased with increasing copper oxidation state. Qin et al. [37] suggested that  $\text{Cu}^{2+}$  was the active site in the  $\text{CuO}$ – $\text{CeO}_2$  system. Nina Perkas et al. [38] indicated that metallic  $\text{Cu}^0$  deposited on  $\text{TiO}_2$  would enhance its activity in CO oxidation, with the  $\text{Cu}^0$  metal serving as both an effective co-catalyst for CO oxidation and a reducing species to react with CO. In the literature, the most active Cu species for a  $\text{CuO}/\text{TiO}_2$ – $\text{SnO}_2$  system in CO oxidation are still under debate.

Many studies have focused on the reaction mechanism of CO oxidation over copper catalysts. Habraken et al. studied the CO– $\text{O}_2$  interaction on Cu (110), (111), and (100) single crystals, concluding that the CO oxidation reaction proceeded via a Langmuir–Hinshelwood (LH) mechanism involving adsorbed CO molecules and oxygen atoms [39,40]. This is supported by the results obtained by Choi and Vannice [32]. They proposed that the catalyst surface is a thin overlayer (two or three monolayers) of  $\text{Cu}_2\text{O}$  with  $\text{O}_2$  vacancies under reaction conditions, which allows the adsorption of CO on exposed  $\text{CuO}$  species, or possibly on  $\text{Cu}_2\text{O}/\text{Cu}$  interface sites, while  $\text{O}_2$  interacts with Cu atoms to maintain the  $\text{Cu}_2\text{O}$  layer. By contrast, Boon et al. emphasized the oxygen vacancies in copper oxide for the oxidation of CO [41]. However, studies on the reaction mechanism of rutile-type oxygen-ion-conducting oxide supports with base metal catalytic agents for CO oxidation are lacking. As a result, although studies have proven that CO oxidation activity over copper supported on  $\text{TiO}_2$ – $\text{SnO}_2$  is significantly enhanced, its mechanism remains poorly understood.

Our group has been working on this topic for many years, by systematically studying the coordination states and reduction properties of  $\text{CuO}/\text{WO}_3/\text{CeO}_2$ ,  $\text{CuO}/\text{Fe}_2\text{O}_3$ ,  $\text{CuO}/\text{Ti}_{0.5}\text{Sn}_{0.5}\text{O}_2$ , and  $\text{CuO}/\text{t-ZrO}_2$  catalysts [25,42–44]. Accordingly, the present work elucidates the structural characteristics; the dispersion, reduction, and adsorption/desorption behaviors; and the activity of the representative  $\text{CuO}/\text{TiO}_2$ – $\text{SnO}_2$  catalysts. The following aspects were studied in detail: (1) the dispersion and state of copper oxide on the  $\text{Ti}_x\text{Sn}_{1-x}\text{O}_2$  surface; (2) the surface structure of the  $\text{CuO}/\text{Ti}_x\text{Sn}_{1-x}\text{O}_2$  catalysts and the structure–property relationship; (3) the interaction of CO and/or  $\text{O}_2$  with the copper-based catalyst, to understand the influence of  $\text{SnO}_2$  doping on the variation of copper species and adsorbed CO and/or  $\text{O}_2$  species; and (4) comparison of CO conversion in the presence and absence of water vapor. These results would help illustrate CO oxidation over copper oxide supported on  $\text{TiO}_2$ – $\text{SnO}_2$ .

## 2. Experimental

### 2.1. Catalyst preparation

$\text{Ti}_x\text{Sn}_{1-x}\text{O}_2$  mixed oxides were prepared by coprecipitation. The requisite amounts of  $\text{TiCl}_4$  and  $\text{SnCl}_4 \cdot 5\text{H}_2\text{O}$  (the molar ratio of  $\text{Ti}/\text{Sn} = 1:3$ ,  $1:1$ , and  $3:1$ ) solutions were mixed. Ammonia solution was added dropwise to these solutions while stirring vigorously. The resulting precipitate was dried at 110 °C for 12 h, and it was then calcined at 450, 600, 850, and 1200 °C for 4 h in flowing air.

The  $\text{CuO}/\text{Ti}_x\text{Sn}_{1-x}\text{O}_2$  samples were prepared by impregnating  $\text{Ti}_x\text{Sn}_{1-x}\text{O}_2$  with an aqueous solution containing 5 wt.% of  $\text{Cu}(\text{NO}_3)_2$ . The samples were dried at 110 °C for 12 h and then calcined in air at 450 °C for 4 h. For simplicity, these synthesized samples were denoted as 5CuTxSy-T. For example, 5CuT3S1-600 represented a molar ratio of  $\text{Ti}/\text{Sn}$  of 3:1, a calcination temperature of 600 °C, and a CuO loading of 5 wt.%.

### 2.2. Catalyst characterization

#### 2.2.1. X-ray diffraction

X-ray diffraction (XRD) patterns were obtained with a Philips X'pert Pro diffractometer equipped with a high-temperature chamber using Ni-filtered  $\text{CuK}\alpha$  radiation (0.15418 nm). The X-ray tube was operated at 40 kV and 40 mA.

#### 2.2.2. Brunauer–Emmett–Teller surface areas

The Brunauer–Emmett–Teller (BET) surface areas were measured by nitrogen adsorption at 77 K on a Micromeritics ASAP-2020 adsorption apparatus.

#### 2.2.3. Laser Raman spectra

Laser Raman spectroscopy (LRS) was performed with a Renishaw Invia Raman spectrometer. An  $\text{Ar}^+$  laser was used to produce Raman excitation at 514.5 nm. Raman spectra were obtained by co-adding three scans of 20 s at a resolution of  $4\text{ cm}^{-1}$  and a laser power of 20 mW under ambient conditions.

#### 2.2.4. Temperature-programmed reduction

$\text{H}_2$ -temperature-programmed reduction (TPR) was carried out in a quartz U-tube reactor, and 50 mg of the sample was used for each measurement. Before reduction, the sample was pretreated in a  $\text{N}_2$  stream at 100 °C for 1 h and then cooled to room temperature. Then the sample was passed through a  $\text{H}_2$ – $\text{Ar}$  mixture (7%  $\text{H}_2$  by volume), with a linear increase in temperature at a rate of  $10^\circ\text{C min}^{-1}$ .  $\text{H}_2$  consumption was analyzed using a thermal conductivity detector.

#### 2.2.5. Temperature-programmed desorption

$\text{O}_2$ -temperature-programmed desorption (TPD) was also carried out in the fixed-bed flow reactor. The catalyst (100 mg) was pretreated in helium at 200 °C for 1 h, and then oxygen adsorption was conducted under an  $\text{O}_2$ – $\text{He}$  mixture (20%  $\text{O}_2$  by volume) at 200 °C for 0.5 h. After cooling to room temperature, the system was purged in  $\text{He}$  ( $60\text{ ml min}^{-1}$ ) for 1 h. After the treatment, the temperature was raised to 700 °C at a rate of  $10^\circ\text{C min}^{-1}$  in the helium flow ( $60\text{ ml min}^{-1}$ ), and the effluent gases from the reactor were analyzed with a Balzers Omnistar benchtop mass spectrometer.

#### 2.2.6. X-ray photoelectron spectroscopy

X-ray photoelectron spectroscopy (XPS) experiments were performed on a PHI 5000 Versa Probe high-performance electron spectrometer, using monochromatic  $\text{Al K}\alpha$  radiation (1486.6 eV) at an accelerating power of 15 kW. Before the measurement, the sample was outgassed at room temperature in an ultrahigh-vacuum (UHV) chamber ( $<5 \times 10^{-7}$  Pa). The sample charging effects were compensated by calibrating all binding energies (BEs) with the adventitious C 1s peak at 284.6 eV. This reference gave BE values with an accuracy of  $\pm 0.1$  eV.

#### 2.2.7. In situ Fourier transform infrared spectroscopy

Fourier transform infrared (FT-IR) spectroscopy was performed using a Nicolet 5700 FT-IR spectrometer at a spectral resolution of  $4.0\text{ cm}^{-1}$ . CO and/or  $\text{O}_2$  adsorption was carried out by exposing a self-supporting wafer of a catalyst (about 10 mg), mounted in a commercial controlled environment chamber (HTC-3), to a stream of  $\text{CO-N}_2$  (10% CO by volume) and/or  $\text{O}_2$ – $\text{N}_2$  (20%  $\text{O}_2$  by volume) at a rate of  $5.0\text{ ml min}^{-1}$  for 30 min. The IR spectra were recorded at various target temperatures.

### 2.3. Activity measurement for CO oxidation

The activities of the 5CuTxSy catalysts in the  $\text{CO} + \text{O}_2$  reaction were measured in a flow micro-reactor with a gas composition of

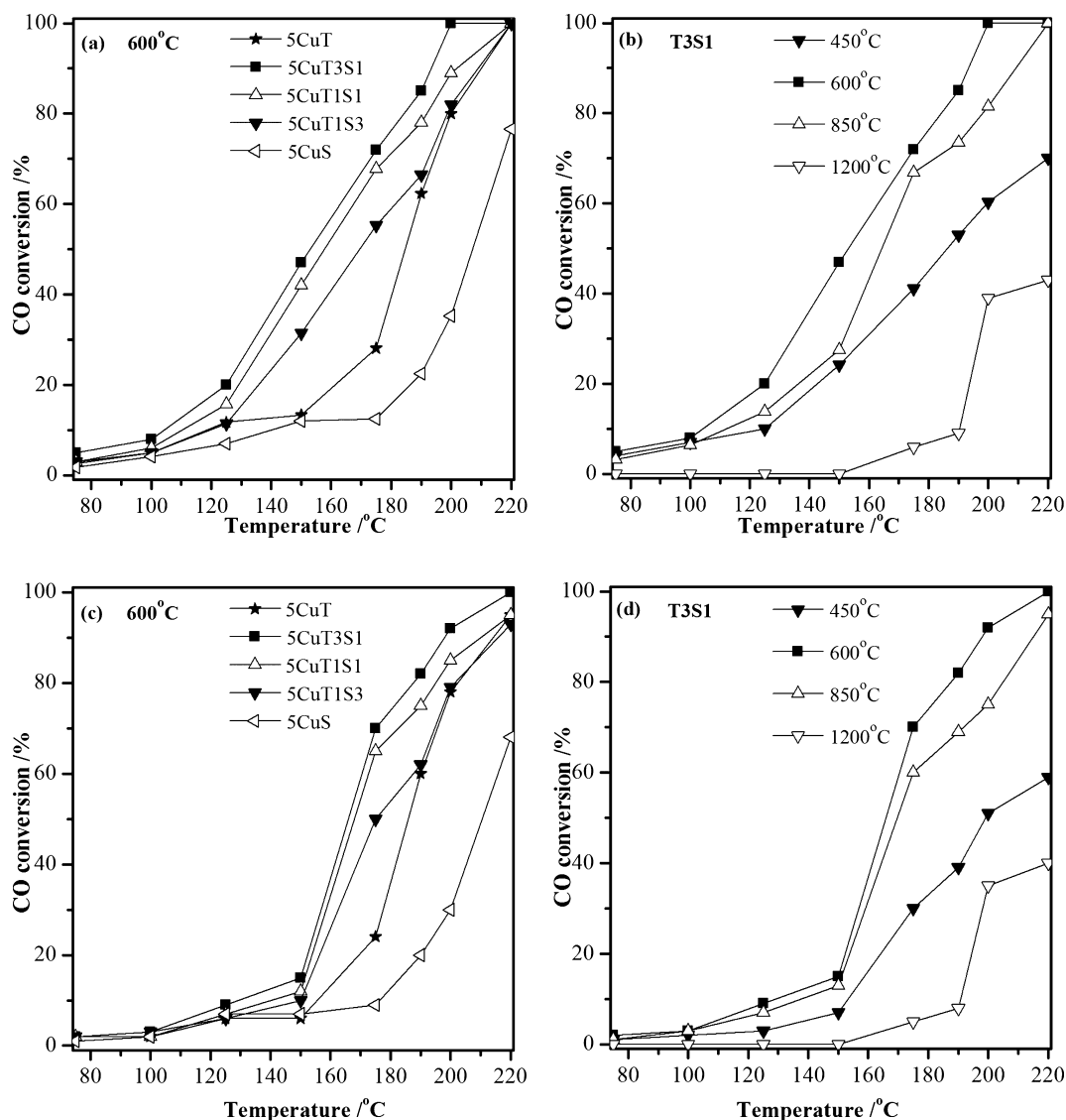


**Fig. 1.** CO conversion (%) over (a) 5CuTxSy-600 °C, (b) 5CuT3S1-T catalysts, (c) 5CuTxSy-600 °C in the presence of water vapor, and (d) 5CuT3S1-T catalysts in the presence of water vapor at various operating temperatures (50–250 °C). x, y, and T are shown in the figure.

1.6% CO, 20.8% O<sub>2</sub>, and 77.6% N<sub>2</sub> by volume at a space velocity of 30,000 mL g<sup>-1</sup> h<sup>-1</sup>; 25 mg of catalyst was used for each measurement. The catalysts were pretreated in a N<sub>2</sub> stream at 100 °C for 1 h before being passed through the reaction gas stream. The tail gas was analyzed using a gas chromatograph with a thermal conductivity detector. Two columns were used for gas separation: one was packed with a 13X molecular sieve (30–60 M) for separating O<sub>2</sub>, N<sub>2</sub>, and CO, the other was packed with Porapak Q for separating CO<sub>2</sub>. In addition, the activities of each catalyst were tested in the absence and presence of 10 vol.% of water vapor. The water vapor (10 vol.%) was introduced into the reaction mixture when studying the effect of H<sub>2</sub>O on the catalytic performance.

### 3. Results and discussion

#### 3.1. Activities of catalysts

The activities of the Cu/Ti<sub>x</sub>Sn<sub>1-x</sub>O<sub>2</sub> catalysts are shown in Fig. 1. The activities of the catalysts are closely related to the titanium oxide content, and they decrease in the order of 5CuT3S1 > 5CuT1S1 > 5CuT1S3 > 5CuT > 5CuS, as shown in Fig. 1a.

For the 5CuT3S1 catalysts, the activities decrease in the order of 5CuT3S1-600 > 5CuT3S1-850 > 5CuT3S1-450 > 5CuT3S1-1200, as shown in Fig. 1b. The 5CuT3S1-600 catalyst showed the best reactivity for the catalytic oxidation of CO, providing a total CO oxidation at 200 °C. Due to the lower copper oxide loading (5% CuO), higher temperatures were observed than in the relevant studies [29,30].

Conversely, large amounts of water vapor (10–15%) are present in the exhaust gas from natural gas vehicles, which strongly affect the activity of the catalyst. Therefore, it is essential to test the performance of these catalysts in the presence of H<sub>2</sub>O in the stream. Fig. 1c,d show the CO conversions of CuO/TiO<sub>2</sub>-SnO<sub>2</sub> catalysts with the addition of H<sub>2</sub>O. As can be seen, the activity of all catalysts substantially decreases at lower temperatures (≤150 °C). At higher temperatures, the CO conversion decreases more slowly. These results suggest that H<sub>2</sub>O vapor over CuO/TiO<sub>2</sub>-SnO<sub>2</sub> catalysts has a negative effect at lower temperatures (≤150 °C). At higher temperatures (≥175 °C), the catalyst shows good resistance to H<sub>2</sub>O during CO oxidation. To further study the reason underlying the difference in catalytic performance, a series of characterizations were carried out for these samples, and the corresponding results are given in the following sections.

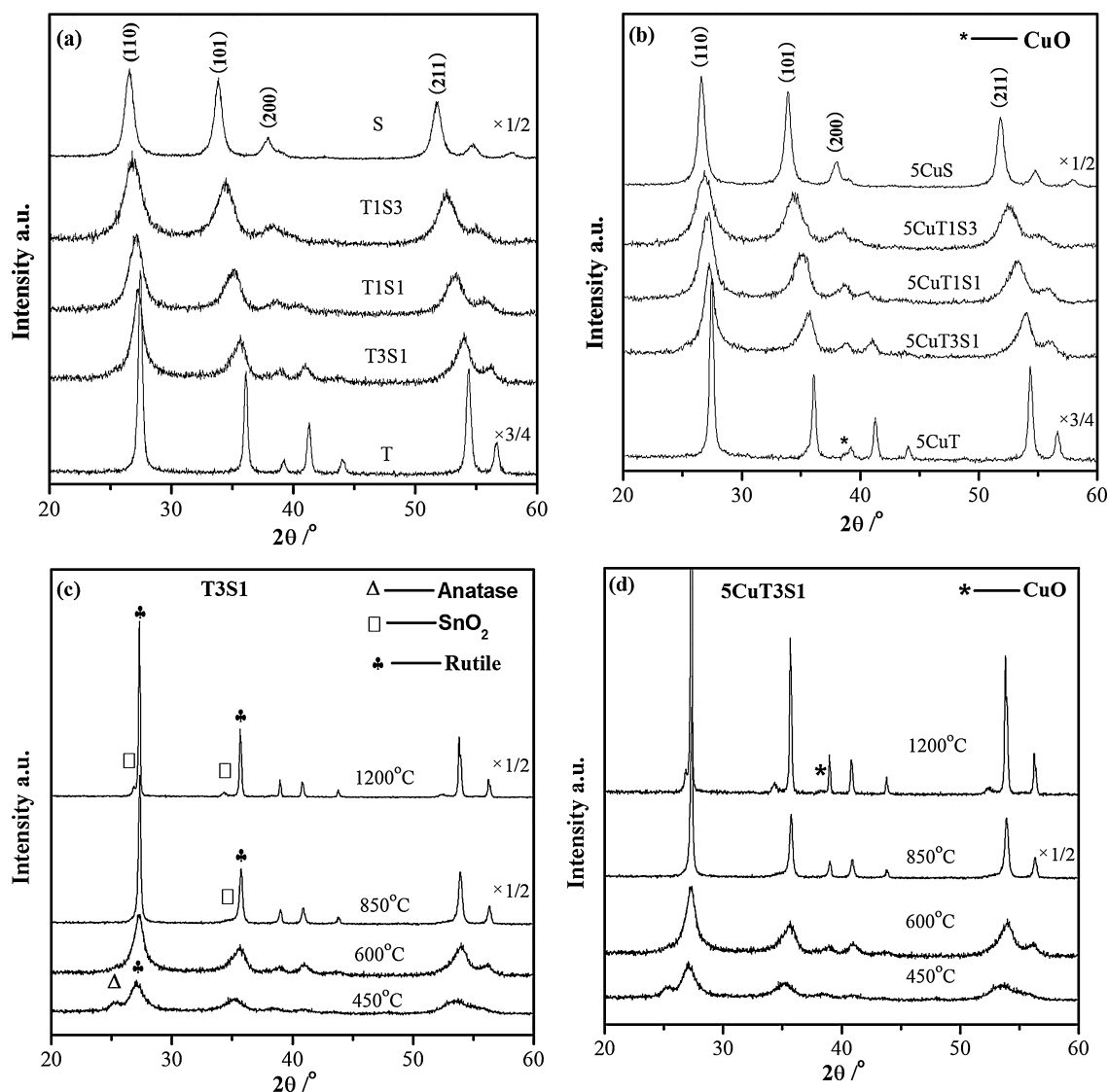


Fig. 2. XRD patterns of (a) Txsy-600°C, (b) 5CuTxsy-600°C, (c) T3S1-T, and (d) 5CuT3S1-T catalysts. x, y, and T are shown in the figure.

### 3.2. Structural and textural characteristics (XRD and LRS)

Fig. 2 displays the XRD patterns of the Txsy-600 and 5CuTxsy-600 samples along with pure SnO<sub>2</sub> and TiO<sub>2</sub> (rutile). For the Txsy samples calcined at 600°C, only the broad diffraction lines of SnO<sub>2</sub> and/or TiO<sub>2</sub> (rutile) are detected. Furthermore, the diffraction peaks of Txsy-600 are slightly shifted to lower angles compared with TiO<sub>2</sub> (rutile), indicating that the interplanar distance increases according to the Bragg equation,  $2d \sin \theta = n\lambda$ . This is consistent with the increase in lattice parameters (Table 1), which is attributed to the substitution of larger-size Sn<sup>4+</sup> (0.071 nm) for Ti<sup>4+</sup> (0.068 nm). These results indicate the successful incorporation of Sn<sup>4+</sup> the TiO<sub>2</sub> lattice to form a uniform solid solution (containing -Ti<sup>4+</sup>-O-Sn<sup>4+</sup>-species) while maintaining the rutile-type structure, which is in agreement with the literature [45]. Moreover, compared with the SnO<sub>2</sub> and TiO<sub>2</sub> (rutile) samples, the diffraction peaks of these Txsy-600 mixed oxides are broadened, suggesting smaller particle sizes of crystallites for Txsy-600 mixed oxides, as tabulated in Table 1. For the CuO-containing catalyst (Fig. 2b), for example, the 5CuT sample, weak diffraction peaks for crystalline CuO (typically at 38.7°C) (JCPDS (Card No. 41-0254)) appear, indicating the formation of some crystalline CuO on the surface of TiO<sub>2</sub>. The diffraction peaks are not observed in other patterns, indicat-

ing that the copper oxide species are highly dispersed and/or are present as small clusters that cannot be easily detected by XRD. This can be attributed to the high surface area of the Txsy support, as shown in Table 1.

Fig. 2c shows the XRD patterns of the T3S1-T samples calcined at various temperatures. The intensities of the diffraction of the rutile structure increased remarkably with the increase in calcination temperature, a result of better crystallization and fewer defects. It is worth noting that the typical diffraction peaks of TiO<sub>2</sub> (anatase) are observed at 450°C. This indicates that the anatase phase does not completely transform into the rutile phase at low temperatures. Phase separation and indexing of these diffraction patterns are observed at 850 and 1200°C, suggesting the formation of two phases. These two phases can be assigned to the individual SnO<sub>2</sub> and the single-phase mixed oxides. Moreover, the lattice parameter of the T3S1-850 and T3S1-1200 samples decreases slightly, further confirming the SnO<sub>2</sub> precipitation. Consequently, we conclude that TiSnO<sub>2</sub> mixed oxides are unstable and undergo spinodal decomposition at high temperatures, for example, 850 and 1200°C, in this study. The XRD patterns of the 5CuT3S1-T samples are shown in Fig. 2d. For samples calcined at 450, 600, and 850°C, only the peaks associated with the corresponding T3S1 samples are detected in the XRD patterns, which implies that copper oxide is well dispersed on

**Table 1**  
Crystallite size, lattice parameter, and BET surface area of these TxSy samples.

Samples	Crystalline size (nm)	Lattice parameter $a = b, c$ (nm)	Lattice volume (nm <sup>3</sup> )	BET surface area (m <sup>2</sup> g <sup>-1</sup> )
TiO <sub>2</sub>	105.5	$a = 0.4587$ $c = 0.2953$	0.0621	16
T3S1	23.9	$a = 0.4608$ $c = 0.3008$	0.0638	67
T1S1	16.2	$a = 0.4663$ $c = 0.3044$	0.0662	80
T1S3	27.5	$a = 0.4706$ $c = 0.3124$	0.0692	71
SnO <sub>2</sub>	28.1	$a = 0.4740$ $c = 0.3188$	0.0716	42
T3S1-450	20.7	$a = 0.4656$ $c = 0.3040$	0.0659	85
T3S1-850	147.2	$a = 0.4600$ $c = 0.2997$	0.0634	23
T3S1-1200	200.3	$a = 0.4595$ $c = 0.2995$	0.0632	9

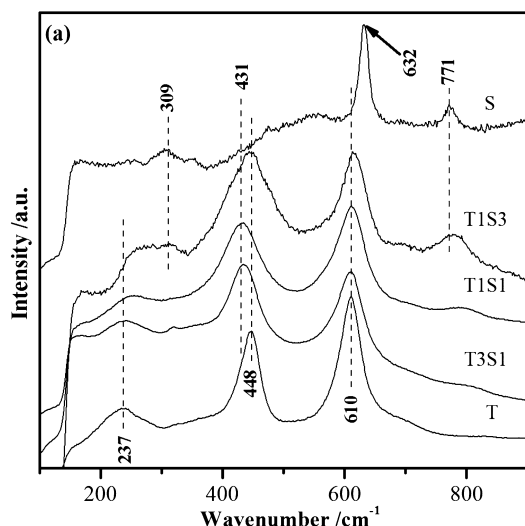


**Fig. 3.** Raman spectra of (a) TxSy-600 °C, (b) 5CuTxSy-600 °C, (c) T3S1-T, and (d) 5CuTxSy-600 °C catalysts. x, y, and T are shown in the figure.

the T3S1 support. However, the diffraction peaks for crystalline CuO appear in the sample calcined at 1200 °C, suggesting that CuO is dispersed less because of its considerably smaller BET area (Table 1). Combined with the activity results, the low activity in the 5CuT3S1-450 sample may be explained by the formation of TiO<sub>2</sub> (anatase). Copper oxide loaded on the TiO<sub>2</sub> (rutile) exhibits a higher activity than that on TiO<sub>2</sub> (anatase) [46]. The low activity in the 5CuT3S1-850 and 5CuT3S1-1200 samples may be a result of the small BET area and the spinodal decomposition at high temperatures.

Among the catalysts, the 5CuT3S1-1200 and 5CuT catalysts exhibit the best H<sub>2</sub>O resistance, whereas the 5CuT3S1-450 and 5CuT1S1 samples show the worst H<sub>2</sub>O resistance. As Table 1 has shown that the 5CuT3S1-1200 and 5CuT catalysts possess small BET surface area, we attribute their H<sub>2</sub>O resistance to the BET surface area. In addition, the 5CuT3S1-450 and 5CuT1S1 samples with larger BET area show the worst activity, proving that small BET surface area enhances H<sub>2</sub>O resistance. This has also been reported in previous studies [47].

Fig. 3a shows the laser Raman spectra of the TxSy-600 samples. The Raman spectrum of TiO<sub>2</sub> (rutile) exhibits three very intense bands at 237, 448, and 610 cm<sup>-1</sup> (B<sub>1g</sub>, E<sub>g</sub>, and A<sub>1g</sub>, respectively). The T3S1 and T1S1 spectra are very similar to that of the pure TiO<sub>2</sub>, confirming the formation of mixed oxides (e.g., solid solution). However, the bands assigned to the SnO<sub>2</sub> phase at 309 and 771 cm<sup>-1</sup> (see SnO<sub>2</sub> spectrum) appears in the spectrum of the T1S3 sample. These bands can still be observed after CuO loading, but their intensities decrease and the peaks broaden compared with those of pure supports, as shown in Fig. 3b. This may be attributed to the interaction with copper oxide species and the disorder in the oxygen sublattice [48]. In addition, the Raman shift of E<sub>g</sub> decreases significantly from 448, 431, 431, and 448 to 433, 402, 402, and 443 cm<sup>-1</sup> for the 5CuTiO<sub>2</sub>, 5CuT3S1, 5CuT1S1, 5CuT1S3,

5CuSnO<sub>2</sub> samples, and the 5CuT3S1 and 5CuT1S1 spectra exhibit the largest shifts. However, the Raman shift of A<sub>1g</sub> (610 cm<sup>-1</sup>) is almost unchanged. Simultaneously, the intensity of E<sub>g</sub> increases and that of A<sub>1g</sub> decreases relatively. This phenomenon may be explained as follows: the two oxygen ions positioned at C<sub>4</sub> axis of the oxygen octahedron are related to the E<sub>g</sub> vibration mode (insert of Fig. 3b). Because one or two oxygen ions can be easily lost under reduction conditions [28], the variation frequency and intensity of the E<sub>g</sub> mode may be seriously affected. Accordingly, we suggest that the presence of more oxygen vacancies on the surface of the 5CuTxSy samples.

The profiles of the heat-treated samples at different temperatures (Fig. 3c) are very similar to those of the T3S1-600 sample. For the sample calcined at 450 °C, a very intense band of the anatase phase appears at 154 cm<sup>-1</sup>, indicating that the anatase and rutile phase coexist at this temperature. For the 850 and 1200 °C samples, the Raman peaks of A<sub>1g</sub> (610 cm<sup>-1</sup>) are shifted from 610 to 616 cm<sup>-1</sup>, suggesting the formation of crystal SnO<sub>2</sub>, which is in good agreement with the XRD results. When the copper oxide is introduced, the Raman shifts and intensities of E<sub>g</sub> and A<sub>1g</sub> are similar to the 5CuT3S1-600 sample, and the E<sub>g</sub> peak of the 600 °C sample shifts the most. These results indicate that the surface of TxSy-T supports have several oxygen vacancies, and the oxygen of CuO occupies these vacancies after the introduction of CuO. The Cu–O–Ti (Sn) band is thus formed, which may result in the transfer of electrons between Cu and Ti (Sn) ions. The larger the E<sub>g</sub> peak shift, the more Cu–O–Ti (Sn) bands are formed.

### 3.3. Redox behaviors and O<sub>2</sub>-TPD studies

The reducing properties of the Cu/Ti<sub>x</sub>Sn<sub>1-x</sub>O<sub>2</sub> samples are characterized by H<sub>2</sub>-TPR, and the results are shown in Fig. 4. The shapes of these TPR profiles are very similar. To further investigate the surface copper oxide species, all the profiles are fitted by Gaussian function, which are also shown in Fig. 4. All of them can be divided into three reduction peaks (labeled as H1, H2, and H3). The two peaks at the low-temperature region (H1 and H2) are mainly attributed to the stepwise reduction of surface-dispersed copper oxide species, that is, Cu<sup>2+</sup> → Cu<sup>+</sup> and Cu<sup>+</sup> → Cu<sup>0</sup> [42,43,49], whereas the other peak at the high-temperature region (H3) may be mainly assigned to the reduction of the surface Ti<sup>4+</sup> (Sn<sup>4+</sup>) of supports, crystalline CuO, or the CuO that interacts strongly with the support [50].

The detailed information of these reduction peaks is summarized in Table 2. The temperature of the reduction peaks H1 of the 5CuTxSy-600 samples increases in the following order: 5CuT = 5CuT3S1 < 5CuT1S1 < 5CuT1S3 < 5CuS. Meanwhile, the temperature of the reduction peaks H2 increases in the order of 5CuT3S1 < 5CuT = 5CuT1S1 < 5CuT1S3 < 5CuS. It follows then that the presence of SnO<sub>2</sub> diminishes the reducing property of the catalysts, due to the different interactions between copper oxide species and the corresponding support, that is, the formation of the Cu–O–Ti (Sn) band. Intrinsically, because the electronegativity of the elements present in the samples are in the order of Ti (1.54) < Cu

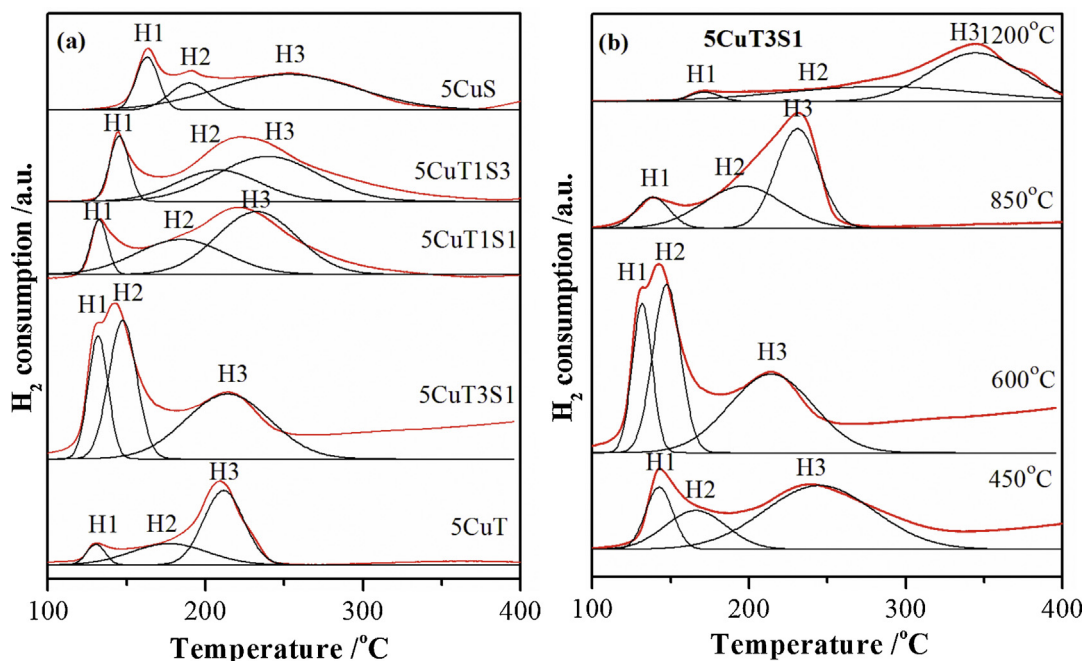


Fig. 4. TPR profiles of (a) 5CuTxSy-600 °C and (b) 5CuT3S1-T catalysts. x, y, and T are shown in the figure.

Table 2

The information of H<sub>2</sub>-TPR and O<sub>2</sub>-TPD over these TxSy catalysts.

Samples	T <sub>H1</sub> (°C)	T <sub>H2</sub> (°C)	T <sub>H3</sub> (°C)	Area of peaks H1 + H2	T <sub>O2</sub> (°C)	Area of peaks O1	Area of peaks O2
5CuS	163	189	252	21.4	158.9	24.2	25.7
5CuT1S3	144	205	240	36.3	158.9	48.0	45.8
5CuT1S1	132	171	232	38.2	198.4	66.6	56.7
5CuT3S1	131	147	214	59.5	150.5	42.3	61.6
5CuT	131	171	211	19.0	190.0	19.8	25.8
5CuT3S1(450)	142	167	239	31.9	147.0	72.3	45.3
5CuT3S1(850)	139	192	231	34.3	381.2	10.3	47.7
5CuT3S1(1200)	170	252	346	25.3	–	–	–

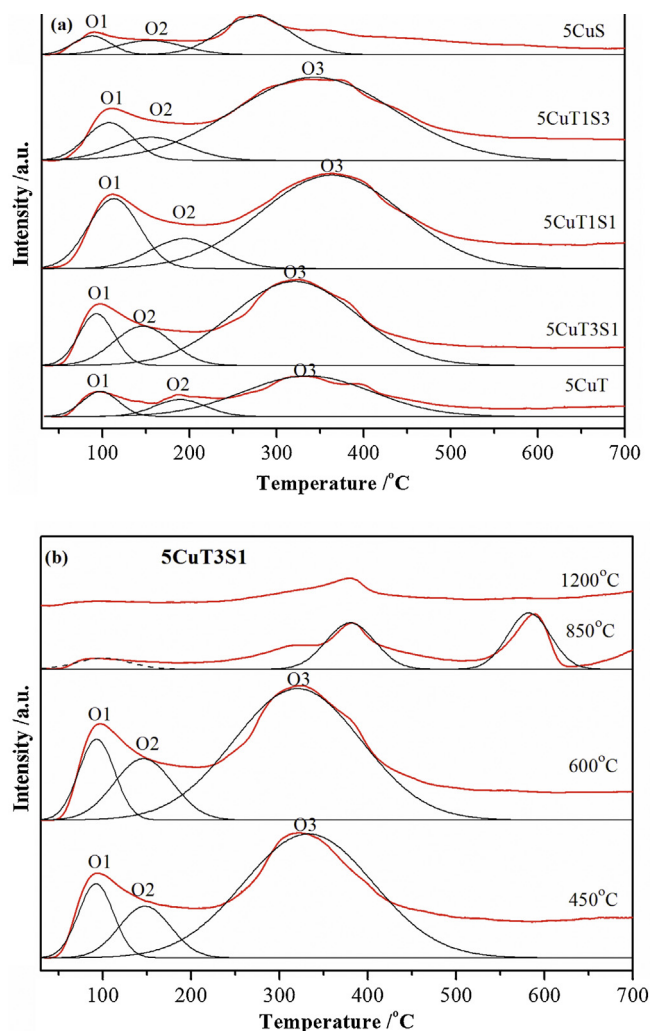
(1.9) < Sn (1.96), the electrons can be captured by Cu<sup>2+</sup> in these samples through the Cu–O–Ti link, while the electrons are donated to Sn<sup>4+</sup>; consequently, the reduction of CuO in 5CuS is very difficult. Moreover, it is worth noting that the peak areas of H1 + H2 decrease in the order of 5CuT3S1 > 5CuT1S1 > 5CuT1S3 > 5CuS > 5CuT, suggesting that more CuO is reduced and more O<sub>2</sub> is adsorbed on the oxygen vacancies in the 5CuT3S1 sample than the other samples. This further illustrates the presence of more oxygen vacancies on the surface of the T3S1-600 support. These results are in good agreement with the LRS results, and the oxygen of CuO occupying the oxygen vacancy is more easily reduced.

Table 2 also shows that the 5CuT3S1-T samples calcined at various temperatures present three reduction peaks, but the reduction of surface CuO is weakened at low temperatures due to high-temperature calcination. As a result, few defect sites are present on the surface of the samples, that is, the surface oxygen vacancy. Interestingly, the temperature of the reduction peaks of the 5CuT3S1-450 sample is higher than that of the 5CuT3S1-600 sample, which is attributed to the presence of anatase TiO<sub>2</sub> in the 5CuT3S1-450 sample; as reported previously, the CuO cannot be easily reduced on the surface of anatase [46].

The O<sub>2</sub>-TPD experiments were carried out to gain insight into the nature of the surface oxygen species possibly involved in CO oxidation. According to the literature [51], the desorption peaks at temperatures lower than 500 °C are generally ascribed to superficial oxygen species that are weakly bound to the surface. Such species are known to participate in oxidation reactions by means

of a superficial mechanism [52]. As shown in Fig. 5, except the 5CuT3S1-1200 sample, all the other samples display three prominent characteristic peaks centered at ca. 100, 200, and 300 °C, respectively. The first peak, often referred to as O1-oxygen, is ascribed to the physically adsorbed oxygen species weakly bound to the surface, which are easily desorbed at low temperatures [53]. The second peak, O2-oxygen, is associated with O<sub>2</sub><sup>–</sup> species formed by the adsorbed O<sub>2</sub> on the surface vacancies [52]. The third peak, O3-oxygen, possibly results from the lattice oxygen O<sup>2–</sup> species on the sample surface [52]. The former two desorption peaks must be investigated further, as they are likely to participate in the oxidation reactions.

The oxygen-supplying ability depends on the number of oxygen-supplying centers and activity [44]. The information of these desorption peaks is summarized in Table 2. No regular trend in change is observed in the amount of O1-oxygen species, but it is sequentially consistent with the BET area, suggesting that the large specific surface area aids in the adsorption of O<sub>2</sub> as physically adsorbed oxygen. However, the amount of O2-oxygen species decreases in the order of 5CuT3S1 > 5CuT1S1 > 5CuT1S3 > 5CuT > 5CuS. Noticeably, a close correlation between the catalytic activity and the concentration of O<sub>2</sub><sup>–</sup> oxygen species indicates that the large amount of reactive O<sub>2</sub><sup>–</sup> oxygen species is chiefly responsible for enhanced CO oxidation activity. For the 5CuT3S1-T samples (see Fig. 5b), with increasing the calcination temperature, the O2-oxygen species peak significantly decreases with increasing calcination temper-



**Fig. 5.** O<sub>2</sub>-TPD spectra of (a) 5CuTxSy-600 °C and (b) 5CuT3S1-T catalysts. x, y, and T are shown in the figure.

ature. Moreover, the amount of O<sub>2</sub><sup>−</sup> species released from the 5CuT3S1-1200 sample is almost undetectable.

In fact, many researchers have proposed electrophilic oxygen species to be the key oxidant in CO oxidation [54]. However, the results seem contradictory to the general notion of lattice oxygen oxidizing CO. In this work, the adsorbed O<sub>2</sub><sup>−</sup> species is considered to be the main species responsible for enhancing the activity of the 5CuT3S1-600 sample at very low temperatures (150 °C). It is clear that the present synthesis processing (Sn addition) can allow the effective creation of high density of surface oxygen vacancy, which might play an important role in accelerating the activation and the formation of chemisorbed O<sub>2</sub><sup>−</sup> species.

### 3.4. Chemical states analysis (XPS)

The surface composition and elementary oxidation states are analyzed by XPS. Fig. 6 shows the XPS spectra of Ti 2p, Sn 3d, Cu 2p, and O 1s for the 5CuTxSy-600 sample. The BE of Sn 3d<sub>5/2</sub> and Sn 3d<sub>3/2</sub> was observed at ~486.1 and ~494.6 eV, respectively, indicating that Sn mainly existed as Sn<sup>4+</sup> [48]. Interestingly, the BEs of Sn 3d<sub>5/2</sub> and Sn 3d<sub>3/2</sub> shifted to lower values after the addition of Ti<sup>4+</sup>. This shift proves the existence of Sn with lower valence resulting from the oxygen vacancies. The XPS spectra of Ti 2p are given in Fig. 6. Two peaks corresponding to Ti 2p<sub>3/2</sub> and Ti 2p<sub>1/2</sub> are observed. The peak position corresponding to Ti 2p<sub>3/2</sub> is located

between Ti 2p<sub>3/2</sub> in Ti<sup>4+</sup> (458.7 eV) and Ti 2p<sub>3/2</sub> in Ti<sup>3+</sup> (457.8 eV), and the BEs of Ti 2p<sub>3/2</sub> shifted to lower values with the increase of TiO<sub>2</sub>, further confirming the existence of oxygen vacancies. These results are in agreement with the LRS and O<sub>2</sub>-TPD results, that is, the presence of oxygen vacancies on the surface of the samples. Furthermore, for all the samples, the bulk compositions of these Cu/Ti<sub>x</sub>Sn<sub>1-x</sub>O<sub>2</sub> catalysts were determined by X-ray fluorescence (XRF), and the results are summarized in Table S1. In comparison with the results shown in Table 3, the Ti/Sn ratios by XPS are observed to be slightly higher than those of the bulk composition, suggesting that the surface is enriched with titanium [16]. This, in turn, leads to more oxygen vacancies.

The Cu 2p spectra mostly show Cu<sup>2+</sup> and a small amount of Cu<sup>+</sup>, located at 933.2 and 930.8 eV, respectively [50]. The oxygen vacancy may result in the generation of Cu<sup>+</sup>, and the oxygen of CuO occupies the vacancy and forms the Cu–O–Ti (Sn) band. It is worth noting that the molar ratio of Cu<sup>2+</sup>/Cu<sup>+</sup> is the least in 5CuT3S1 samples (see Table 3), indicating the presence of more Cu<sup>+</sup> ions on this sample surface.

The high-resolution spectrum for the O 1s ionization features is numerically fitted with the Gaussian features, representing the primary O 1s ionization feature and chemically shifted O 1s features from the chemisorbed surface species. The strong band O' (529.9 eV) is attributed to the characteristic O<sup>2−</sup> of the metal oxide surface [54], whereas the shoulder O'' with higher BE (532.1 eV) resulted from the chemisorbed oxygen that formed the O<sub>2</sub><sup>−</sup> species [54], which is in accordance with the O<sub>2</sub>-TPD results. However, the BE of O 1s in these samples is higher than that of 5CuT. This may be because the electronegativity of Sn (1.96) is larger than that of Ti (1.62); that is, the electron-capturing ability of Sn is stronger than that of Ti, which leads to the higher BE of O 1s with the addition of SnO<sub>2</sub>.

For further investigating surface interaction and the chemical state of elements in the near-surface region, XPS is performed on the T3S1-T support calcined at different temperatures. As shown in Fig. 7, for all samples, the valence of tin and titanium is predominantly 4+, and a chemical shift occurred in Sn 3d and Ti 2p with an increase in temperature. Especially for the 5CuT3S1-850 and 5CuT3S1-1200 samples, the Sn 3d and Ti 2p signals shifted chemically to higher BE. These phenomena suggest that calcination has a significant effect on the valence of tin and titanium, such that the sample surface has fewer oxygen vacancies with increasing temperature. It is reasonable that the samples are sintered at increasing temperatures, resulting in fewer defects and oxygen vacancies. Interestingly, calcination leads not only to the chemical shift of Cu 2p<sub>3/2</sub> and Cu 2p<sub>1/2</sub> signals to low BE but also to the decrease in the shake-up peak due to the characteristic Cu<sup>2+</sup>. In addition, except for 5CuT3S1-1200, a shoulder peak appears at 930.3 eV, which is assigned to the reduced state of copper species [50].

Besides the O' (529.9 eV) and O'' (532.1 eV) peaks in the O 1s spectra (Fig. 7), a peak O''' (533.0 eV) appears on the surface due to the formation of oxygen from CO<sub>3</sub><sup>2−</sup> during calcination. Although no chemical shift was found in the O 1s feature with change in the calcination temperature, the intensity of O<sub>2</sub><sup>−</sup> gradually increases in the following order: 600 > 450 > 850 > 1200. This may be caused by the presence of an oxygen vacancy on the oxide surface. This is in accordance with the O<sub>2</sub>-TPD results discussed earlier, most likely because the density of lattice oxygen vacancy is lessened.

### 3.5. CO and/or O<sub>2</sub> interaction with these samples (in situ FT-IR)

To further investigate the effects of the support on the surface-dispersed copper oxide species, the in situ FT-IR spectra of CO adsorption are recorded, as shown in Fig. 8. Generally, the adsorp-

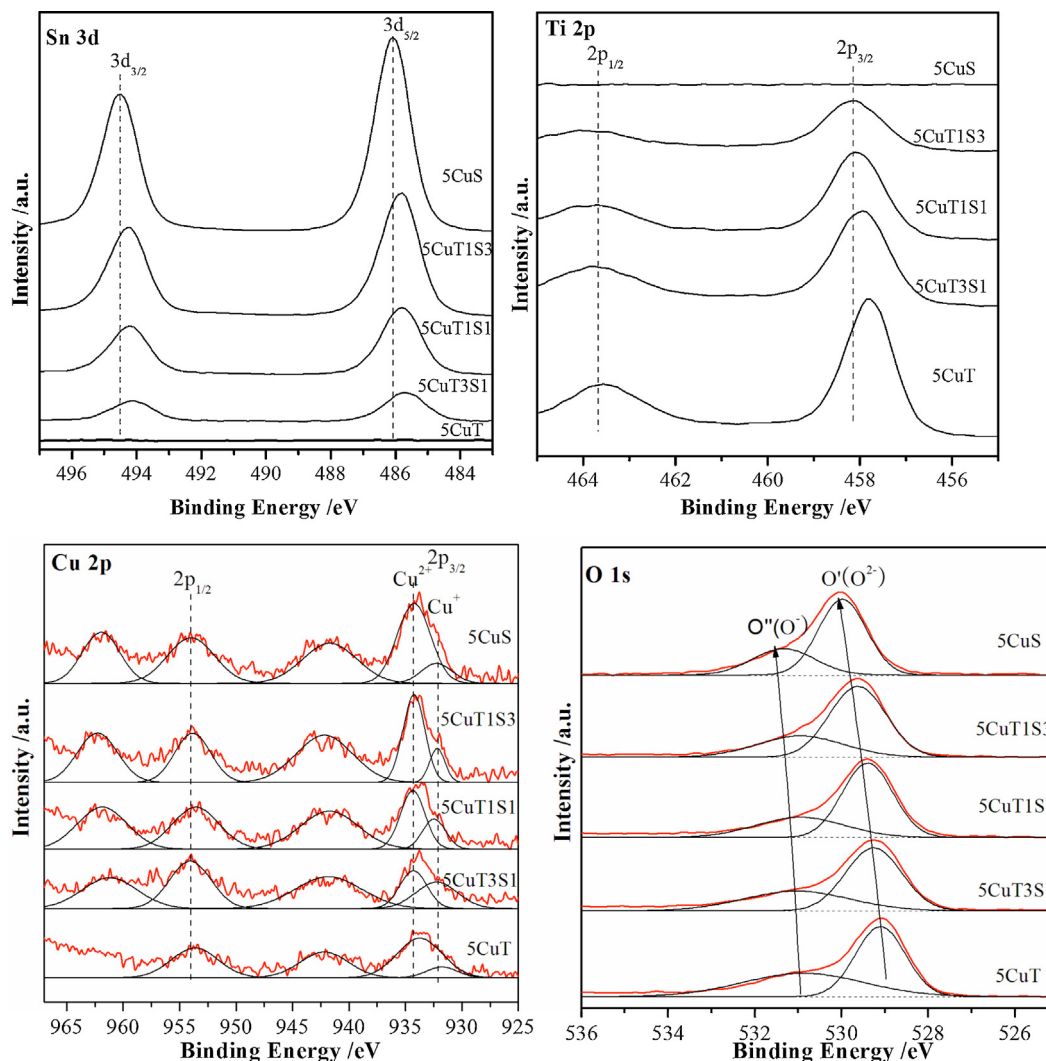


**Fig. 6.** XPS spectra (Sn 3d, Ti 2p, Cu 2p, and O1s) of 5CuTxSy-600 °C catalysts. x and y are shown in the figure.

**Table 3**

The surface compositions of the samples obtained by XPS analysis.

Samples	C1s	O1s	Ti2p	Sn3d5	Cu2p3	Ti/Sn	Cu <sup>2+</sup> /Cu <sup>+</sup>
5CuSn	16.5	54.6		23.2	5.7		7.5
5CuTi	20.2	59.3	17.3		3.2		8.0
CuT3S1(450)	20.5	52.3	15.8	3.6	7.9	4.4	20
CuT3S1(600)	24.0	54.8	13.7	4.1	3.5	3.3	1.3
CuT3S1(850)	32.8	48.1	11.3	3.8	4.1	3.0	80
CuT3S1(1200)	40.6	44.0	7.9	3.2	4.4	2.5	100
CuT1S3(600)	17.7	54.4	7.2	15.5	5.3	0.5	4.0
CuT1S1(600)	19.4	45.5	12.2	9.1	4.9	1.3	2.0

tion of CO molecules on Cu<sup>2+</sup>, Cu<sup>+</sup>, and Cu<sup>0</sup> gives rise to peaks with characteristic vibrational frequencies at about 2220–2150, 2160–2080, and below 2130 cm<sup>−1</sup>, respectively; at the ambient temperature, Cu<sup>+</sup>–CO adsorbs most stably [48]. For all supports, no CO adsorption is observed at 2200–2050 cm<sup>−1</sup> (not shown); thus, the peak at about 2110 cm<sup>−1</sup> in the spectra should be attributed to the vibration of Cu<sup>+</sup>–CO at room temperature. The same features are observed for all samples excluding 5CuT3S1-1200. The peaks of CO adsorption on Cu<sup>+</sup> are evident at room temperature and at higher temperatures. The peak intensities increase gradually and then decrease until they finally disappear. The Cu<sup>+</sup>–CO adsorption peaks at room temperature indicate the presence of some Cu<sup>+</sup> species in

the samples at ambient temperatures. This is in agreement with the XPS results, which suggest the presence of Cu<sup>+</sup> ions on the sample surface. With increasing temperature, the Cu<sup>2+</sup> species are reduced gradually and more Cu<sup>+</sup> ions are formed on the surface of samples, with a resulting gradual increase in peak intensity. As the temperature increases continuously, Cu<sup>+</sup> ions are further reduced to Cu<sup>0</sup>, and the peak intensity decreases gradually until their disappearance. Simultaneously, the CO adsorption peak shifts to a higher wave number (2100 cm<sup>−1</sup> at 25 °C and 2120 cm<sup>−1</sup> at higher temperatures), which can be attributed to the Cu<sup>+</sup>–(CO)<sub>2</sub> adsorption [55]. The initial formation of Cu<sup>+</sup>–CO is followed by insertion of a second CO in the coordination sphere of monocoordinated Cu<sup>+</sup> ions

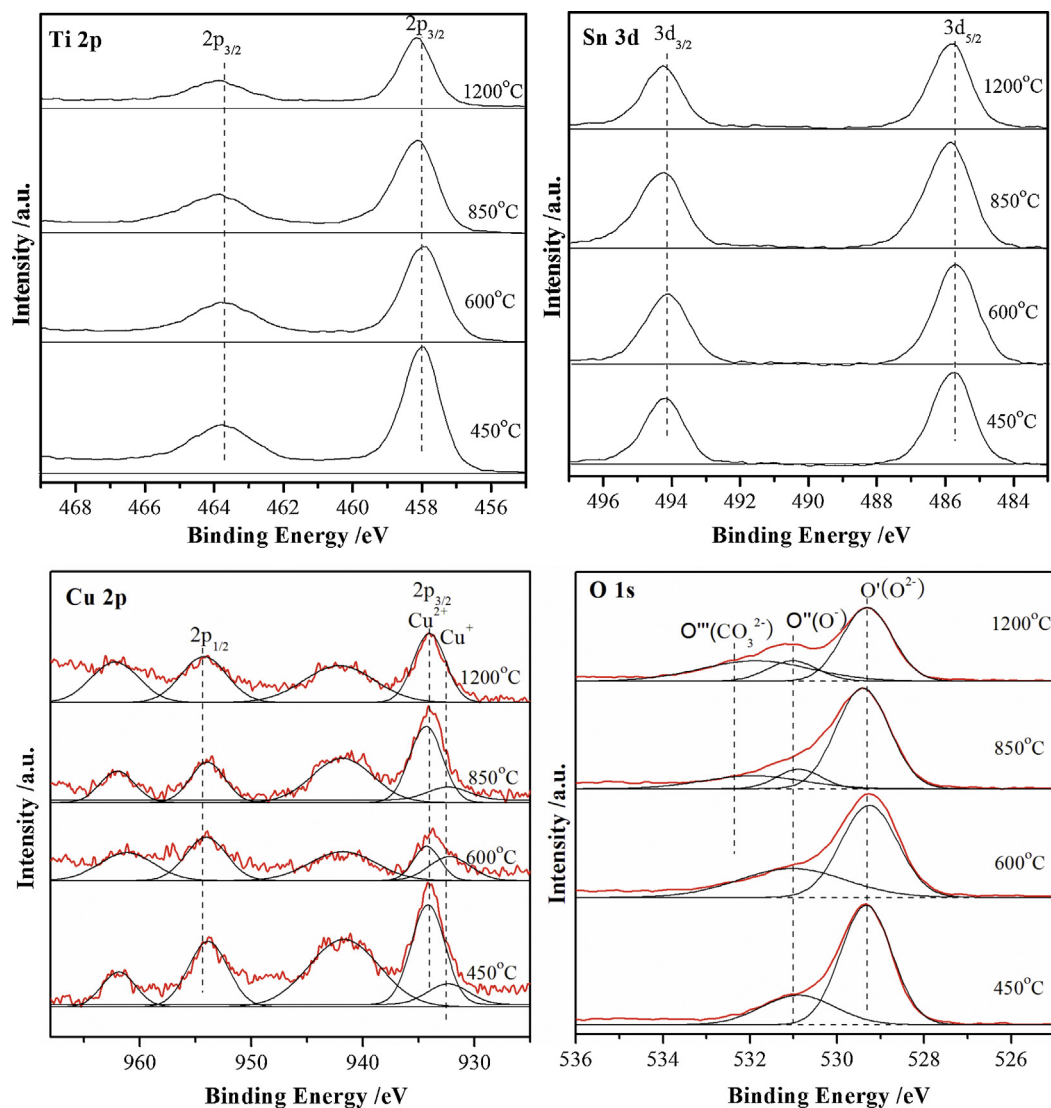
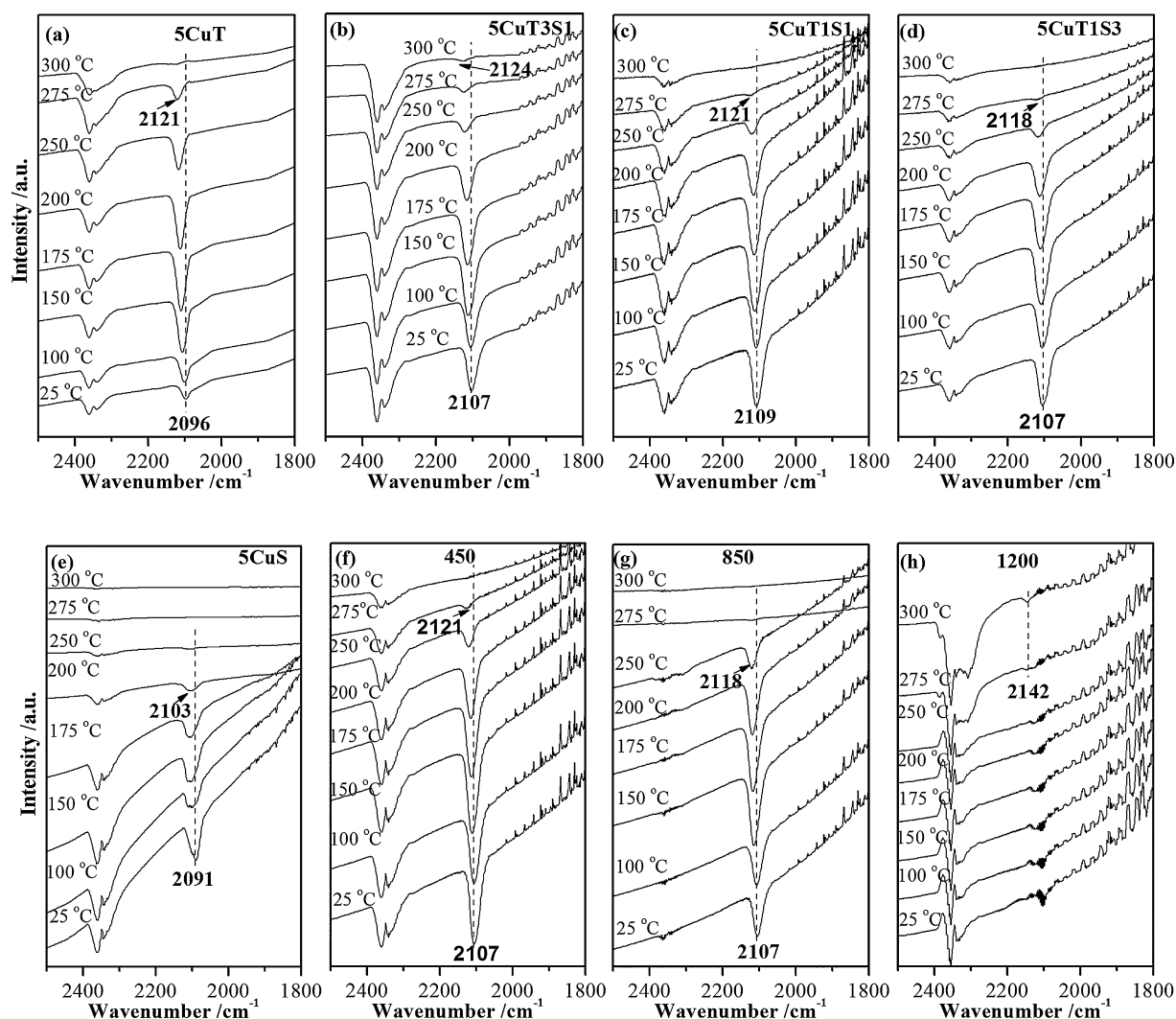


Fig. 7. XPS spectra (Sn 3d, Ti 2p, Cu 2p, and O1s) of 5CuT3S1-T catalysts. T is shown in the figure.

[55]. However, the desorption temperatures of the  $\text{Cu}^+ - \text{CO}$  peaks differ with Ti/Sn ratio and temperature. For the 5CuT, 5CuT1S3, and 5CuT1S1 samples, the maximum peak area of CO adsorption on  $\text{Cu}^+$  appears at about  $150^\circ\text{C}$  and disappears completely at  $300^\circ\text{C}$ . For the 5CuT3S1 sample, the maximum peak area of CO adsorption on  $\text{Cu}^+$  appears at about  $150^\circ\text{C}$ , and the desorption process is very slow, which can be observed even at  $300^\circ\text{C}$ . For the 5CuS sample, the peak intensity remains unchanged at lower temperatures, but it disappears completely at  $250^\circ\text{C}$ . It can be concluded that the CO adsorption on 5CuT3S1 is much more stable than others; that is,  $\text{Cu}^+$  is much more stable in 5CuT3S1, which can provide more CO adsorption sites, than in the other samples. For the 5CuT3S1-450 and 5CuT3S1-850 samples, the maximum peak area of CO adsorption on  $\text{Cu}^+$  appears at about  $150^\circ\text{C}$  and disappears completely at  $300^\circ\text{C}$ . However, for the 5CuT3S1-1200 sample, no CO adsorption appears, indicating that the reduction of  $\text{Cu}^{2+}$  to  $\text{Cu}^+$  is difficult, which is in agreement with the  $\text{H}_2$ -TPR results.

In order to study the surface reaction mechanism further, the in situ FT-IR spectra of CO and  $\text{O}_2$  co-adsorption are recorded while simulating the  $\text{CO} + \text{O}_2$  reaction, as shown in Fig. 9. Taking the 5CuS, 5CuT3S1-600, 5CuT, and 5CuT3S1-1200 as examples, all samples are found to differ. For the 5CuS, 5CuT3S1-600, and 5CuT samples, the peaks of CO adsorption on  $\text{Cu}^+$  appear at room temperature, as

indicated by the peak at  $2110\text{ cm}^{-1}$ . However, the peak is weaker in intensity than that of CO adsorption, indicating that  $\text{O}_2$  molecules preferentially adsorb on the surface of the sample, thus occupying surface vacancies. As such, the adsorption of CO is inhibited. In this situation, free gaseous CO can react with the adsorbed  $\text{O}_2^-$  species slowly. Furthermore, the band for  $\text{CO}_2$  ( $2360\text{ cm}^{-1}$ ) is very weak, suggesting that the reaction activity may be very low. The peak at  $2110\text{ cm}^{-1}$  suddenly disappears with the increase in temperature, and a new peak appears at around  $2142\text{ cm}^{-1}$  due to the  $\text{Cu}^+ - (\text{CO})_2$  adsorption, indicating that  $\text{Cu}^+ - (\text{CO})_2$  species can be formed in the presence of the reaction gas, which may contribute to the activity of the  $\text{CO} + \text{O}_2$  reaction. It is also worth noting that the band for  $\text{CO}_2$  ( $2360\text{ cm}^{-1}$ ) shows an obvious increase, suggesting the rapidity of the reaction. The intensity of the band for  $\text{CO}_2$  ( $2360\text{ cm}^{-1}$ ) increases significantly with a further increase in temperature, suggesting that a possible increase in reaction activity. These results further explain why  $\text{Cu}^+ - (\text{CO})_2$  species play a very important role in the  $\text{CO} + \text{O}_2$  reaction. Interestingly, for the 5CuS, 5CuT3S1-600, and 5CuT samples,  $\text{Cu}^+ - (\text{CO})_2$  species are formed at  $200^\circ\text{C}$ ,  $150^\circ\text{C}$ , and  $200^\circ\text{C}$ , respectively. This is in agreement with the activity results. The 5CuT3S1-600 sample exhibits high activity at  $150^\circ\text{C}$ , and the CO conversion reaches ca. 50%. By contrast, the activities of the 5CuS and 5CuT samples reach ca. 50% at higher temperatures.



**Fig. 8.** IR spectra following an exposure of 5CuTxSy-600 °C and 5CuT3S1-T catalysts to CO stream at different temperatures. The samples and the adsorption temperatures are shown in the figure.

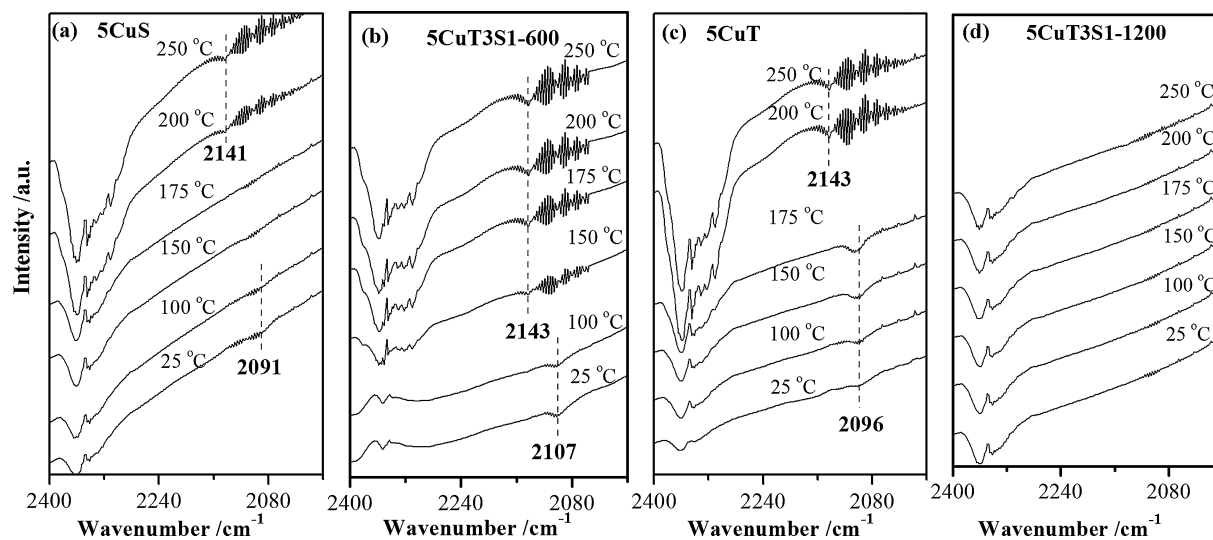


**Fig. 9.** IR spectra following an exposure of representative 5CuTxSy catalysts to CO+O<sub>2</sub> stream at different temperatures. The samples and the adsorption temperatures are shown in the figure.

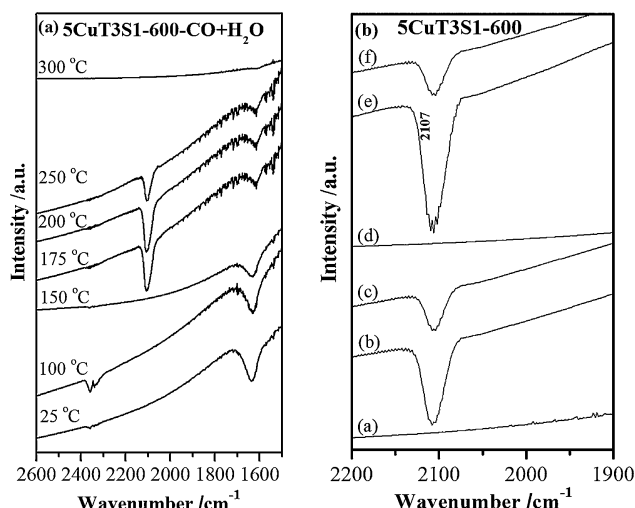


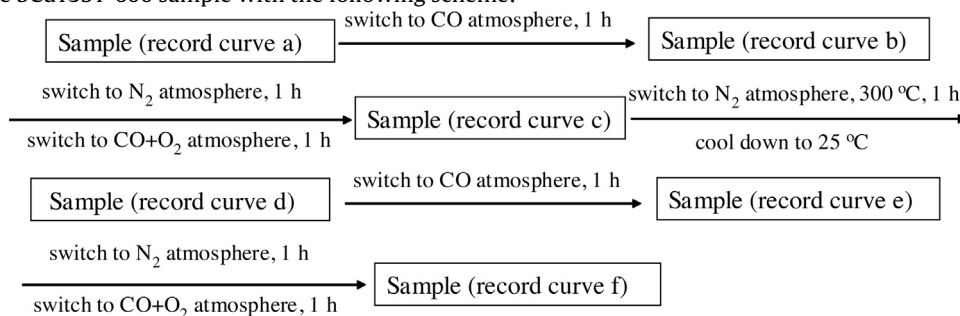
**Fig. 10.** (a) IR spectra following an exposure of 5CuT3S1-600 °C catalysts to CO + H<sub>2</sub>O stream at different temperatures; (b) IR spectra following an exposure of 5CuT3S1-600 °C catalyst to different gas streams and pretreated conditions.

At the temperature adopted here, no Cu<sup>+</sup>–CO species can be detected in the 5CuT3S1-1200 sample, indicating that no Cu<sup>+</sup> species exists on the sample surface. In other words, during the reaction, the CO cannot adsorb on the surface, resulting in low activity. In line with this, no significant change is observed in the band for CO<sub>2</sub> (2360 cm<sup>−1</sup>).

To further investigate the effects of water vapor on CO oxidation, the in situ FT-IR spectra of CO + H<sub>2</sub>O co-adsorption in the 5CuT3S1-600 sample are recorded, as shown in Fig. 10a. In the presence of H<sub>2</sub>O, the peaks of H<sub>2</sub>O adsorption appear at 1630 cm<sup>−1</sup>, and no CO adsorption peak is observed. The competitive adsorption of H<sub>2</sub>O and CO on the catalysts and the blockage of the active sites by water vapor possibly explain the decrease in activity in the presence of H<sub>2</sub>O. However, when the reaction temperature is increased, the H<sub>2</sub>O peak gradually decreases and disappears. Simultaneously, the CO peak appears and rises steadily. This result suggests that H<sub>2</sub>O addition limits the adsorption of CO, in turn leading to a decrease in catalytic activity at lower temperatures. Gurbani et al. [56] proposed the poisoning effect of H<sub>2</sub>O on CO oxidation catalysts.

### 3.6. Possible reaction mechanism of CO oxidation over the 5CuTxSy catalysts

For investigating the reaction mechanism further, the FT-IR experiments (shown in Fig. 10b) were continuously performed over the 5CuT3S1-600 sample with the following scheme:



The spectrum (b) of Cu<sup>+</sup>–CO is observed at 2107 cm<sup>−1</sup> when the sample is exposed to the CO stream at 25 °C for 1 h. However, the Cu<sup>+</sup>–CO peak weakens in comparison with spectrum b when the sample is exposed to the CO + O<sub>2</sub> stream at 25 °C for 1 h. This indicates that O<sub>2</sub> first adsorbs on the surface of the catalyst and then forms the O<sub>2</sub><sup>−</sup> species, resulting in the conversion of Cu<sup>+</sup> to Cu<sup>2+</sup>, in

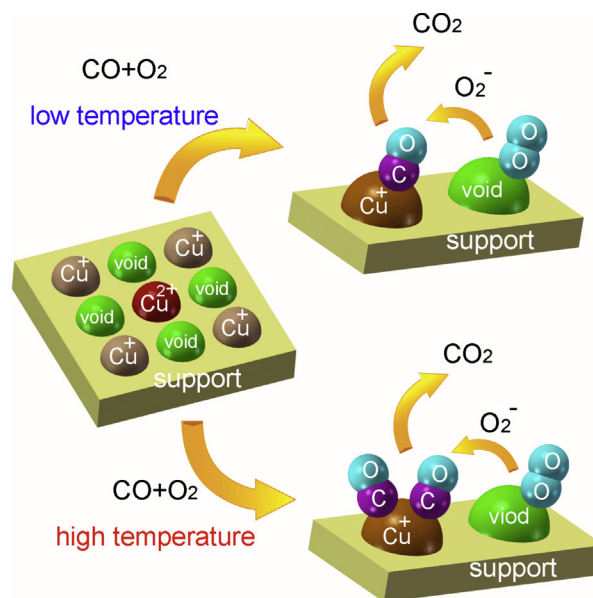


**Fig. 11.** Possible reaction mechanism for CO oxidation over 5CuTxSy-T catalysts.

turn weakening the CO adsorption. Conversely, adsorbed O<sub>2</sub> prevents the adsorption of CO. To further explain this phenomenon, the FT-IR spectroscopy of CO and CO + O<sub>2</sub> adsorption was performed after pretreatment of the sample at 300 °C under a N<sub>2</sub> atmosphere. It can be seen that the peak of CO adsorption for the spectra c and d is obviously stronger than the fresh sample. Meanwhile, the peak of CO + O<sub>2</sub> co-adsorption is similar to the non-pretreated sample. This result further proves that O<sub>2</sub> first adsorbs on the surface of the catalyst, and then it forms the O<sub>2</sub><sup>−</sup> species, ultimately weakening the CO adsorption.

Following the previous characterizations, a possible reaction mechanism (schematic diagram) of CO oxidation under the current conditions is proposed to further illustrate this reaction (Fig. 11). Based on the in situ FT-IR results of CO and O<sub>2</sub> co-adsorption, the reaction of CO + O<sub>2</sub> over these 5CuTxSy-T samples proceeds via the same reaction pathway, which is an LH mechanism. In addition, the results in this study indicate that the 5CuT3S1-600 sample is better than the other samples for the CO + O<sub>2</sub> reaction. As a result, with the 5CuT3S1-600 sample as an example, the electrons can migrate from Ti<sup>4+</sup> and Sn<sup>4+</sup> to Cu<sup>2+</sup> for generation of Cu<sup>+</sup> at room temperature (25 °C). This is because the electronegativity of Cu is larger than that of Ti, which is supported by the in situ FT-IR results of XPS and CO adsorption. When the catalyst is exposed to a gas mix-

ture of CO and O<sub>2</sub> at 25 °C, O<sub>2</sub> molecules are preferentially adsorbed on the surface of the catalyst to form O<sub>2</sub><sup>−</sup> species in the oxygen vacancy. This behavior inhibits the adsorption of CO species, thus weakening the CO adsorption peak. Furthermore, below 150 °C, the CO molecules adsorbed on Cu<sup>+</sup> can react with the O<sub>2</sub><sup>−</sup> species to

produce small amounts of CO<sub>2</sub>. On increasing the temperature up to 150 °C, Cu<sup>+</sup>–(CO)<sub>2</sub> species are formed and more CO molecules are adsorbed on the surface of the catalyst. The adsorbed CO can quickly react with O<sub>2</sub><sup>–</sup> species to produce more CO<sub>2</sub>, which is in agreement with the in situ FT-IR results on the catalytic activity and CO + O<sub>2</sub> co-adsorption.

#### 4. Conclusions

In this work, a series of CuO/Ti<sub>x</sub>Sn<sub>1–x</sub>O<sub>2</sub> catalysts were prepared to investigate the relationships between surface structure and the catalytic performance of the CO oxidation reaction. The following major conclusions were obtained:

(1) For the Ti<sub>x</sub>Sn<sub>1–x</sub>O<sub>2</sub> mixed oxides, the incorporation of Sn<sup>4+</sup> into the lattice of TiO<sub>2</sub> leads to a decrease in the crystallite size of TiO<sub>2</sub> and an increase in lattice strain. CuO species can be highly dispersed on Ti<sub>x</sub>Sn<sub>1–x</sub>O<sub>2</sub> supports, forming many surface Cu<sup>+</sup> ions and oxygen vacancies, which are important for catalytic performance.

(2) The reducing property of the catalysts (mainly CuO species) is affected by the Ti/Sn ratio and the thermal treatment of the supports. The CuO/Ti<sub>0.75</sub>Sn<sub>0.25</sub>O<sub>2</sub> catalyst calcined at 600 °C exhibits better reducing ability, resulting in more surface Cu<sup>+</sup> species and oxygen vacancies being formed in the reaction atmosphere, thus showing the best catalytic activity.

(3) CO species can adsorb on Cu<sup>+</sup> forming Cu<sup>+</sup>–(CO)<sub>2</sub>, and O<sub>2</sub><sup>–</sup> is formed by the adsorption of O<sub>2</sub> on the oxygen vacancy. The adsorbed CO reacts with O<sub>2</sub><sup>–</sup> to produce CO<sub>2</sub>.

(4) The H<sub>2</sub>O-resistant activity of catalysts is dependent on the BET surface area and the ability of H<sub>2</sub>O to adsorb on the surface of catalysts.

#### Acknowledgements

The financial supports of National Nature Science Foundation of China (Nos. 20973091, 21273110), National Basic Research Program of China (973 program, Nos. 2010CB732300, 2012CB21500203), the China Postdoctoral Science Foundation (No. 2014M550451), the Nature Science Foundation of Guangxi Province (No. 2014GXNSFBA118036), the Project of Guangxi Key Laboratory of Petrochemical Resource Processing and Process Intensification Technology (Nos. 2013K009, 2013Z001), the Project of Guangxi Postdoctoral Special Foundation (Nos. Y304002007, B41054) are gratefully acknowledged.

#### Appendix A. Supplementary data

Supplementary data associated with this article can be found, in the online version, at <http://dx.doi.org/10.1016/j.apcatb.2015.06.034>

#### References

- [1] W. Liu, M. Flytzani-Stephanopoulos, *J. Catal.* 153 (1995) 304–332.
- [2] Y. Choi, H.G. Stenger, *J. Power Sour.* 129 (2004) 246–254.
- [3] P. Nonam, P. Myung-June, H. Kyoung-Su, L. Yun-Jo, J. Ki-Won, *Fuel* 129 (2014) 163–172.
- [4] M. Kurnatowska, W. Mistaa, P. Mazurb, L. Kepinski, *Appl. Catal. B: Environ.* 148–149 (2014) 123–135.
- [5] Y. Denkwitz, A. Karpenko, V. Plzakb, R. Leppelt, B. Schumacher, R.J. Behma, *J. Catal.* 246 (2007) 74–90.
- [6] J. Dae-Woon, J. Won-Jun, S. Jae-Oh, H. Won-Bi, R. Hyun-Seog, H.J. Un, L.Y. Wang, *Renew. Energy* 65 (2014) 102–107.
- [7] R.V. Gulyaev, E.M. Slavinskaya, S.A. Novopashin, D.V. Smovzh, A.V. Zaikovskii, D.Y. Osadchii, O.A. Bulavchenko, S.V. Korenev, A.I. Boronin, *Appl. Catal. B: Environ.* 147 (2014) 132–143.
- [8] Z.L. Wu, D.E. Jiang, A.K.P. Mann, D.R. Mullins, Z.A. Qiao, L.F. Allard, C.J. Zeng, R.C. Jin, S.H. Overbury, *J. Am. Chem. Soc.* 136 (2014) 6111–6122.
- [9] X.N. Li, Z. Yuan, S.G. He, *J. Am. Chem. Soc.* 136 (2014) 3617–3623.
- [10] G.L. Zhou, H. Lan, T.T. Gao, H.M. Xie, *Chem. Eng. J.* 246 (2014) 53–63.
- [11] L. Qi, Q. Yu, Y. Dai, C.J. Tang, L.J. Liu, H.L. Zhang, F. Gao, L. Dong, Y. Chen, *Appl. Catal. B: Environ.* 119–120 (2012) 308–320.
- [12] D.A. Svintitskiy, T.Y. Kardash, O.A. Stonkus, E.M. Slavinskaya, A.I. Stadnichenko, S.V. Koscheev, A.P. Chupakhin, A.I. Boronin, *J. Phys. Chem. C* 117 (2013) 14588–14599.
- [13] A.P. Jia, G.S. Hu, L. Meng, Y.L. Xie, J.Q. Lu, M.F. Luo, *J. Catal.* 289 (2012) 199–209.
- [14] J.L. Cao, Y. Wang, T.Y. Zhang, S.H. Wu, Z.Y. Yuan, *Appl. Catal. B: Environ.* 78 (2008) 120–128.
- [15] R. Lin, M.F. Luo, Y.J. Zhong, Z.L. Yan, G.Y. Liu, W.P. Liu, *Appl. Catal. A: Gen.* 255 (2003) 331–336.
- [16] T.Y. Zhang, S.P. Wang, Y. Yu, Y. Su, X.Z. Guo, S.R. Wang, S.M. Zhang, S.H. Wu, *Catal. Commun.* 9 (2008) 1259–1264.
- [17] Z.Q. Zou, M. Meng, L.H. Guo, Y.Q. Zha, J. Hazard. Mater. 163 (2009) 835–842.
- [18] A.P. Jia, S.Y. Jiang, J.Q. Lu, M.F. Luo, *J. Phys. Chem. C* 114 (2010) 21605–21610.
- [19] A. Kubacka, R. Si, P. Michorczyk, A. Martínez-Arias, W.Q. Xu, J.C. Hanson, J.A. Rodríguez, M. Fernández-García, *Appl. Catal. B: Environ.* 132–133 (2013) 423–432.
- [20] S.Y. Yao, K. Mudiyansele, W.Q. Xu, A.C. Johnston-Peck, J.C. Hanson, T.P. Wu, D. Stacchiola, J.A. Rodríguez, H.Y. Zhao, K.A. Beyer, K.W. Chapman, P.J. Chupas, A. Martínez-Arias, R. Si, T.B. Bolin, W.J. Liu, S.D. Senanayake, *ACS Catal.* 4 (2014) 1650–1661.
- [21] M.Y. Kang, H.J. Yun, S.J. Yu, W. Kim, N.D. Kim, J. Yi, *J. Mol. Catal. A: Chem.* 368–369 (2013) 72–77.
- [22] B.L. Zhu, X.X. Zhang, S.R. Wang, S.M. Zhang, S.H. Wu, W.P. Huang, *Microporous Mesoporous Mater.* 102 (2007) 333–336.
- [23] S.A. Talipova, V.N. Vorobiev, *React. Kinet. Catal. Lett.* 22 (1986) 469–474.
- [24] E. Moretti, M. Lenarda, L. Storaro, A. Talon, T. Montanari, G. Busca, E. Rodríguez-Castello, A. Jimenez-Lopez, M. Turco, G. Bagnasco, R. Frattini, *Appl. Catal. A: Gen.* 335 (2008) 46–55.
- [25] H.Q. Wan, Z. Wang, J. Zhu, X.W. Li, B. Liu, F. Gao, L. Dong, Y. Chen, *Appl. Catal. B: Environ.* 79 (2008) 254–261.
- [26] D.C. Hurum, A.G. Agrios, K.A. Gray, T. Rajh, M.C. Thurnauer, *J. Phys. Chem. B* 107 (2003) 4545–4549.
- [27] R. Sasikala, N.M. Guptab, S.K. Kulshreshtha, *Catal. Lett.* 71 (2001) 69–73.
- [28] T.C. Lu, L.B. Lin, X.T. Zu, S. Zhu, L.M. Wang, *Nucl. Instrum. Methods Phys. Res. B* 218 (2004) 111–116.
- [29] J. Huang, S.R. Wang, X.Z. Guo, D. Wang, B.L. Zhu, S.H. Wu, *Catal. Commun.* 9 (2008) 2131–2135.
- [30] K.R. Li, Y.J. Wang, S.R. Wang, B.L. Zhu, S.M. Zhang, W.P. Huang, S.H. Wu, *J. Nat. Gas Chem.* 18 (2009) 449–452.
- [31] K.I. Choi, M.A. Vannice, *J. Catal.* 131 (1991) 22–35.
- [32] K.I. Choi, M.A. Vannice, *J. Catal.* 131 (1991) 36–50.
- [33] C.S. Chen, T.C. Chen, C.C. Chen, Y.T. Lai, J.H. You, T.M. Chou, C.H. Chen, *J.F. Lee, Langmuir* 28 (2012) 9996–10006.
- [34] T.J. Huang, D.H. Tsai, *Catal. Lett.* 87 (2003) 173–178.
- [35] F. Severino, J.L. Brito, J. Laine, J.L.G. Fierro, A.L. Agudo, *J. Catal.* 177 (1998) 82–95.
- [36] G.G. Jernigan, G.A. Somorjai, *J. Catal.* 147 (1994) 567–577.
- [37] J.W. Qin, J.F. Lu, M.H. Cao, C.W. Hu, *Nanoscale* 2 (2010) 2739–2743.
- [38] N. Perkas, P. Gunawan, G. Amirian, Z. Wang, Z.Y. Zhong, A. Gedanken, *Phys. Chem. Chem. Phys.* 16 (2014) 7521–7530.
- [39] F.H.P. Habraken, G.A. Bootsma, P. Hofmann, S. Hachicha, A.M. Bradshaw, *Surf. Sci.* 88 (1979) 285–298.
- [40] F.H.P. Habraken, G.A. Bootsma, *Surf. Sci.* 88 (1979) 333–347.
- [41] A.Q.M. Boon, F. van Looij, J.W. Geus, *J. Mol. Catal.* 75 (1992) 277–291.
- [42] H.L. Chen, H.Y. Zhu, Y. Wu, F. Gao, L. Dong, J.J. Zhu, *J. Mole. Catal. A: Chem.* 255 (2006) 254–259.
- [43] X.W. Li, M.M. Shen, X. Hong, H.Y. Zhu, F. Gao, Y. Kong, L. Dong, Y. Chen, *J. Phys. Chem. B* 109 (2005) 3949–3955.
- [44] X.J. Yao, Q. Yu, Z.Y. Ji, Y.Y. Lv, Y. Cao, C.J. Tang, F. Gao, L. Dong, Y. Chen, *Appl. Catal. B: Environ.* 130–131 (2013) 293–304.
- [45] L.B. Kong, J.M.H. Huang, *J. Alloys Compd.* 336 (2002) 315–319.
- [46] H.Y. Zhu, L. Dong, Y. Chen, *J. Colloid Interf. Sci.* 357 (2011) 497–503.
- [47] S.H. Zeng, Y. Wang, S.P. Ding, J.J.H.B. Sattler, E. Borodina, L. Zhang, B.M. Weckhuysen, H.Q. Su, *J. Power Sour.* 256 (2014) 301–311.
- [48] L.H. Dong, L.J. Liu, Y.Y. Lv, J. Zhu, H.Q. Wan, B. Liu, F. Gao, X.S. Wang, L. Dong, Y. Chen, *J. Mol. Catal. A: Chem.* 365 (2012) 87–94.
- [49] P. Zimmer, A. Tschöpe, R. Birringer, *J. Catal.* 205 (2002) 339–345.
- [50] L.H. Dong, L.L. Zhang, C.Z. Sun, W.J. Yu, J. Zhu, L.J. Liu, B. Liu, Y.H. Hu, F. Gao, L. Dong, Y. Chen, *ACS Catal.* 1 (2011) 468–480.
- [51] M. Meng, P.Y. Lin, Y.L. Fu, *Catal. Lett.* 48 (1997) 213–222.
- [52] N.A. Merino, B.P. Barbero, P. Grange, L.E. Cadús, *J. Catal.* 231 (2005) 232–244.
- [53] L. Xue, C.B. Zhang, H. He, Y. Teraoka, *Appl. Catal. B: Environ.* 75 (2007) 167–174.
- [54] Q. Liu, L.C. Wang, M. Chen, Y. Cao, H.Y. He, K.N. Fan, *J. Catal.* 263 (2009) 104–113.
- [55] D. Scarno, S. Bordiga, C. Lamberti, G. Spoto, G. Ricchiardi, A. Zecchina, C.O. Areal, *Surf. Sci.* 411 (1998) 272–285.
- [56] A. Gurbani, J.L. Ayastuy, M.P. González-Marcos, J.E. Herrero, J.M. Guil, M.A. Gutiérrez-Ortiz, *Int. J. Hydrogen Energy* 34 (2009) 547–553.